ORIGINAL RESEARCH ARTICLE

Structure and Texture of Oxide Dispersion Strengthened Alloy 617 for Very High Temperature Applications

M. SIVAKUMAR, SHYAM KANTA SINHA, ARUP DASGUPTA, and SUFYAN M. SHAIKH

High energy mechanically milled Alloy 617 ODS powder was consolidated by Spark Plasma Sintering (SPS) technique and subsequently annealed at 650 °C and 1050 °C (923 K and 1323 K). Microstructure and microtexture evolution during SPS and annealing have been investigated. SPS consolidated sample exhibited heterogeneous microstructure with ultra-fine grains surrounded by coarse grains. Inhomogeneous distribution of plastic deformation induced during ball milling resulted in heterogeneous nucleation and further grain growth during consolidation. The bimodal microstructure is advantageous with coarse grains providing ductility and fine grains providing strength by the Hall–Petch relationship. The bimodal grains structure was also retained during annealing. As-sintered specimen showed ⟨100⟩ texture parallel to the compression axis due to dynamic recrystallization during the SPS process. At 650 °C, annealed sample exhibited ⟨111⟩ annealing texture parallel to compression axis. The texture was randomized in sample annealed at 1050 °C. Precipitation analysis by SEM, XRD and TEM showed the presence of $M_{23}C_6$, M_6C and Al_2O_3 in both As-sintered and annealed samples. Dispersoids analysis showed the presence of fine and uniform $Y_3Al_5O_{12}$, $Y_4Al_2O_9$ and a complex oxide rich in Ni, Y, Al and O. Stress–strain analysis from instrumented indentation test shows higher yield strength for Alloy 617 ODS in comparison with conventional Alloy 617.

https://doi.org/10.1007/s11661-021-06442-y

I. INTRODUCTION

NICKEL-BASED oxide dispersion strengthened (ODS) superalloys are promising candidate materials with excellent creep strength for high-temperature applications in gas turbines and Gen-IV nuclear reactors operating at about 1000 °C.[1–3] Alloy 617 ODS (Y_2O_3) superalloy is one such material that is expected to be stable up to 1000 °C.[4] Alloy 617, a conventional non-ODS variant is not stable at such high temperature due to coarsening of γ' precipitates at 750 °C and dissolution at 900 °C.[5] Thus, to increase its creep strength, Y_2O_3 is dispersed in the Alloy 617 matrix, termed Alloy 617 ODS. Y_2O_3 is chosen because of its thermal stability over a range of temperatures up to 2000 °C.[6] Fine and uniform distribution of dispersoids in the matrix inhibits the dislocation movement, which improves high-temperature mechanical properties.

Alloy 617 ODS is synthesized by mechanical milling of pre-alloyed Alloy 617 and Y_2O_3 powder, followed by consolidation. During mechanical milling, various milling parameters such as revolutions per minute (RPM) and milling duration are optimized to achieve a uniform and fine distribution of dispersoids. The detailed optimization process of the current alloy is reported by us elsewhere.[7] Earlier, we have also reported local shear texture in a single powder particle due to inhomogeneous rolling and compression of the trapped powder particle in between the balls and between the balls and walls of the jar.[8] Various techniques such as Hot Isostatic Pressing (HIP), Spark Plasma Sintering (SPS), and hot extrusion can be used to consolidate the ODS alloy powders.[9–11] In the current study, SPS has been used for the consolidation of the Alloy 617 ODS powder. The technique involves the application of pulsed direct current (DC) through a graphite die set filled with powder to produce Joule heating while pressure is applied simultaneously. This technique has the advantage of a higher heating rate and shorter holding time. The technique is highly time-saving as it can produce appreciable sintering density in a

M. SIVAKUMAR, SHYAM KANTA SINHA, and ARUP DASGUPTA are with the Indira Gandhi Centre for Atomic Research, Homi Bhabha National Institute, Kalpakkam 603 102, India. Contact e-mail: arup@igcar.gov.in SUFYAN M. SHAIKH is with the Indian Institute of Technology Madras, Kalpakkam 600 036, India.

Manuscript submitted February 23, 2021; accepted August 20, 2021.

Article published online September 3, 2021

short time of 10 minutes as compared to the other consolidation techniques such as HIP of few hours. SPS has earlier been employed to consolidate various Fe as well as Ni-based ODS alloys.[12–16]

Microstructure plays a vital role in offering strength to the material. Improvement in high-temperature strength of ODS superalloys is attributed to their particular kind of microstructure with precipitates in grains and grain boundaries along with fine and uniform distribution of the oxide dispersoids in the matrix, the latter being a foreign material in the system. The microstructure of Alloy 617 ODS generally consists of precipitates such as $M_{23}C_6$, M_6C, Al_2O_3 and complex oxides, namely Y–Al–O and Y–Ti–O.[17] It has been reported in the literature that $M_{23}C_6$ and $Y_2Ti_2O_7$ are stable up to 1250 °C[17] in Alloy 617 ODS. It has also been reported that precipitates in conventional Alloy 617, such as TiC and γ', are absent in the ODS counterpart.[18] Alloy 617 ODS exhibited superior strength compared to its conventional alloy in absence of γ' precipitates[19] owing to dispersion strengthening.[20] Thus Alloy 617 ODS derives its high-temperature strength from carbides and dispersoids. However, literature is scarce on microstructural characterization and correlation with mechanical properties of Alloy 617 ODS.[4,17–19] Further, SPS could induce texture along the direction parallel to the applied pressure resulting in a change of anisotropic properties of the material. In many cases, the texture is related to the processing parameters, making texture characterization important in this class of materials.

In the present study, Alloy 617 ODS has been milled in a temperature-controlled high energy ball mill and consolidated by SPS under optimized conditions[7,8] followed by annealing at 650 °C to characterize γ' and at 1050 °C to understand the nature of dispersoids. In essence, this paper aims to establish stability in microstructure at very high temperatures up to 1050 °C. Instrumented hardness is carried out to assess the mechanical property.

II. EXPERIMENTAL METHODS

Prealloyed Alloy 617 water atomized powder from M/S Padmasree Enterprises, India, was mechanically milled with 0.6 wt pct of cubic Y_2O_3 nano powder in a high energy ball mill from Retsch, Emax at a speed of 1000 rpm and with water cooling up to 12 °C (285 K). The morphology, chemical composition of the initial and milled powder have been reported by us elsewhere.[7] Ball to powder ratio was 10:1, and 5 mm diameter stainless steel balls were used. In order to avoid cold welding of powders to the balls and walls of the jar during milling, 2 wt pct of stearic acid was used as a process controlling agent (PCA).[21] The optimized milled powders were consolidated using Dr. Sinter SPS-5000, Fuji Electronic Industrial Co., Japan. The applied pressure was increased sequentially from 0 to 50 MPa using a cylindrical graphite die and punch of 15 mm diameter to transmit the pressure with the simultaneous increase in temperature from room temperature to 1100 °C (1373 K). Consolidation temperature was attained within 15 minutes, with a hold time of 10 minutes. K-type thermocouple attached to the die was used to monitor the temperature. The consolidated product after SPS is referred to as 'As-sintered' and these samples are annealed at 650 °C and 1050 °C (923 K and 1323 K) for 10 hours.

XRD analysis of the consolidated and annealed pellets was carried out using STOE STADI MP X-ray Diffractometer using Cu-K_α radiation (λ = 1.54060 Å) in Bragg-Brentano geometry. Instrumental broadening was calculated by collecting the XRD pattern for a strain-free standard Si sample. Carl Zeiss Sigma 300 field emission scanning electron microscope (SEM) was used to characterize the size and morphology of the powders. Oxford X-Max Silicon Drift Detector attached to the SEM was used to carry out Energy Dispersive Spectroscopy (EDS) microanalysis. Electron Backscattered Diffraction (EBSD) characterization was carried out with Sigma 300 FE-SEM attached with Oxford Instruments make C Swift complementary metal-oxide semiconductor (CMOS) camera, and the EBSD patterns were analyzed by the Aztec 4.0 software. Transmission electron microscope (TEM) samples were prepared by jet-thinning process using 95 pct Methanol and 5 pct Perchloric acid as the electrolyte, while maintaining voltage and temperature at 20 kV and − 20 °C, respectively.

Philips make CM-200 Analytical TEM and C_s-corrected high-resolution STEM (Titan Themis Z G^3, Thermo Fisher Scientific Co. Ltd) operating at 300 kV with a high brightness field emission gun (X-FEG) and S-COR probe corrector (CEOS Co. Ltd.) were used for microstructural characterization of jet thinned samples. ImageJ software and Gatan microscopy suite were used for the analysis of TEM results.

III. RESULTS

Figures 1(a) through (c) shows the Inverse Pole Figure (IPF) map of As-sintered and annealed samples at 650 °C and 1050 °C, respectively. Both As-sintered and annealed samples exhibited bimodal microstructure with a combination of ultra-fine grains and coarse grains. This observation is in agreement with previous reports in ODS alloys during the SPS process.[22, 23] The high magnification IPF map of the 1050 °C annealed samples in Figure 1(d) reveals ultra-fine grains with nano twins. The formation of nano-twin is due to the low stacking fault energy of Ni alloys.[24]

Grain size distributions of As-sintered and annealed samples at 650 °C and 1050 °C are presented in Figures 2(a) through (c), respectively. As-sintered and 650 °C annealed alloys displayed nearly similar grain sizes where fine grain size peaks at 500 nm and larger grains peaks at ~20 to 30 μm. There is a negligible increase in grain size at 1050 °C. It shows that grain growth is stagnated during the annealing process, which is attributed to immobile second phases, such as precipitates and dispersoids.[25] The presence of special boundaries such as coincidence site lattice (CSL)

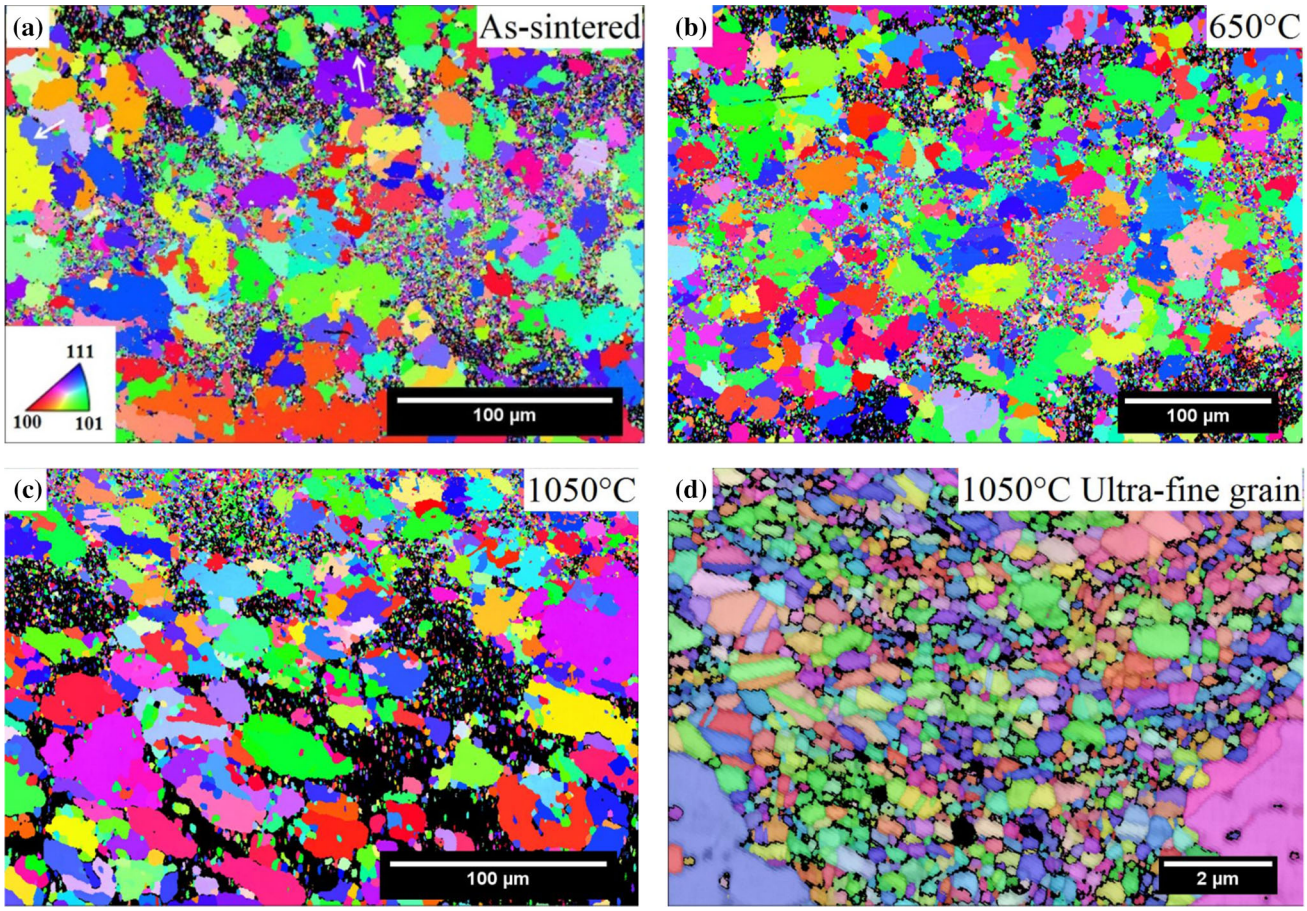

Fig. 1—Inverse pole figure maps of Alloy 617 ODS showing the orientation of crystallographic poles parallel to compression axis of SPS consolidation (*a*) As-sintered, (*b*) annealed at 650 °C, (*c*) annealed at 1050 °C and (*d*) ultra-fine grains at 1050 °C.

boundaries may also inhibit grain growth since it has lower grain boundary energy and less mobility than random boundaries.[26] Ultra-fine grain size at 1050 °C, shown in Figure 2(d) ranges from 0.2 to 1.5 μm with a peak at 0.5 μm.

Figures 3(a) through (c) shows the inverse pole figure (IPF) of As-sintered, 650 °C and 1050 °C annealed samples, respectively, parallel to the axial direction. It is found to be 1.61 to 1.78 times higher than the random texture. IPF of As-sintered alloy tends to show ⟨100⟩ texture parallel to compression axis. During the SPS process, pressure is applied simultaneously with temperature, which may attribute to the ⟨100⟩ dynamic recrystallization texture. Such kind of recrystallization has been observed in ODS alloys during SPS.[22] Similar ⟨100⟩ dynamic texture in Ni–Fe–Cr super alloys has been reported by Coryell *et al.* at high deformation temperature and low strain rate.[27] Dynamic recrystallization is clear from grain boundary bulging, as indicated by arrow mark in Figure 1(a). It has been proposed in the literature that grain boundary bulging is the dominant mechanism for recrystallization at a temperature above 0.5 T/T_m,[28] and this kind of bulging has been reported by Fu *et al.* in Ni-Fe-Cr super alloys.[29] Annealing the As-sintered specimen at 650 °C shows ⟨111⟩ texture parallel to the compression axis. Such kind of annealing texture is reported by Bhattacharjee *et al.* in cross-rolled Ni during annealing due to the formation of annealing twins.[30] At 1050 °C, there is either randomized texture or weak ⟨110⟩ and ⟨100⟩ texture. Texture randomization in nickel-based superalloys has been attributed in the literature been to static $\sum 3$ boundary formation.[29] Further analysis of CSL boundary is carried out to understand the effect on texture.

CSL boundaries are the special type of boundaries with low energy, which improve mechanical properties. Figures 4(a) through (c) represents the CSL boundary map of As-sintered, 650 °C and 1050 °C annealed samples, respectively, and percentages of $\sum 3$, $\sum 5$, and $\sum 7$ type CSL boundaries is shown in Figure 4(d). It is observed that $\sum 3$ boundaries are in higher fractions as compared to other CSL boundaries in As-sintered and annealed samples. The percentage of $\sum 3$ boundaries increased from 20 pct in As-sintered and 650 °C annealed samples to 30 pct in 1050 °C while $\sum 5$ and $\sum 7$ remain the same. It was established in Ni that $\sum 3$ boundary increases during annealing due to grain rotation to minimize the system energy.[31] This increase in the fraction of $\sum 3$ boundaries at 1050 °C further weakened the texture. Such kind of weakening of texture

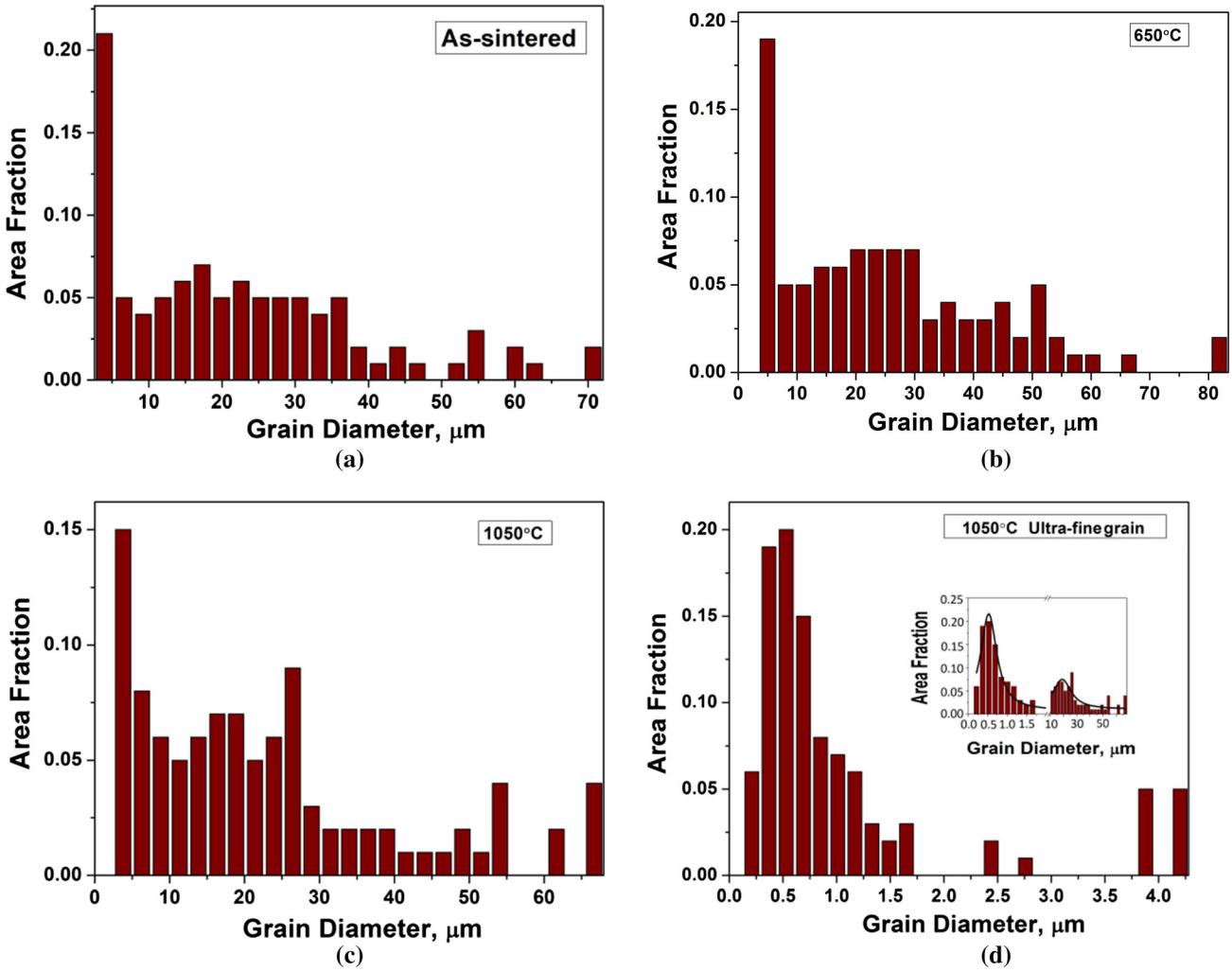

Fig. 2—Grain size distribution of Alloy 617 ODS (*a*) As-sintered, (*b*) annealed at 650 °C, (*c*) annealed at 1050 °C and (*d*) ultra-fine grains at 1050 °C, respectively (inset with distinct ultra-fine and coarse grains showing bimodal distribution at 1050 °C from high and low resolution IPF maps).

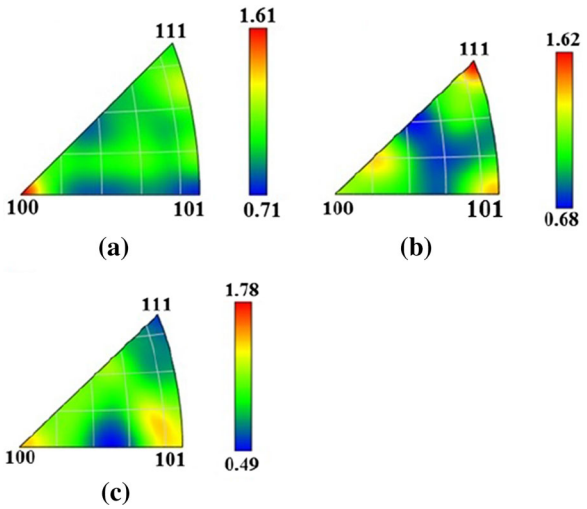

Fig. 3—Inverse pole figure (IPF) of Alloy 617 ODS parallel to compression axis of SPS consolidation (*a*) As-sintered, (*b*) annealed at 650 °C and (*c*) annealed at 1050 °C.

with an increase in $\sum 3$ boundaries is reported by Fu *et al.* in nickel-based superalloys.[29]

Kernel average misorientation (KAM) map analysis is carried out to characterize the spatial distribution of stored energy. Figures 5(a) through (c) shows the KAM map of As-sintered, 650 °C and 1050 °C annealed samples, respectively. Corresponding legend is given in Figure 5(d). It is observed from Figures 5(a) through (c) that there is limited misorientation in the coarse grains and more concentration of misorientation (green color) in the ultra-fine grains. The linear relationship between the misorientation and dislocation density allows the direct comparison of deformation level.[22] Thus the fine grains are partially recovered grains, and the coarse grains are recrystallized and grown grains. Recovery occurs more slowly in low to medium stacking fault energy materials such as Ni-based superalloys.[27]

Figure 6(a) and (b) shows the back scattered electron (BSE) micrograph of As-sintered samples at lower and higher magnifications, respectively. It is observed from the micrograph that the entire matrix is covered with

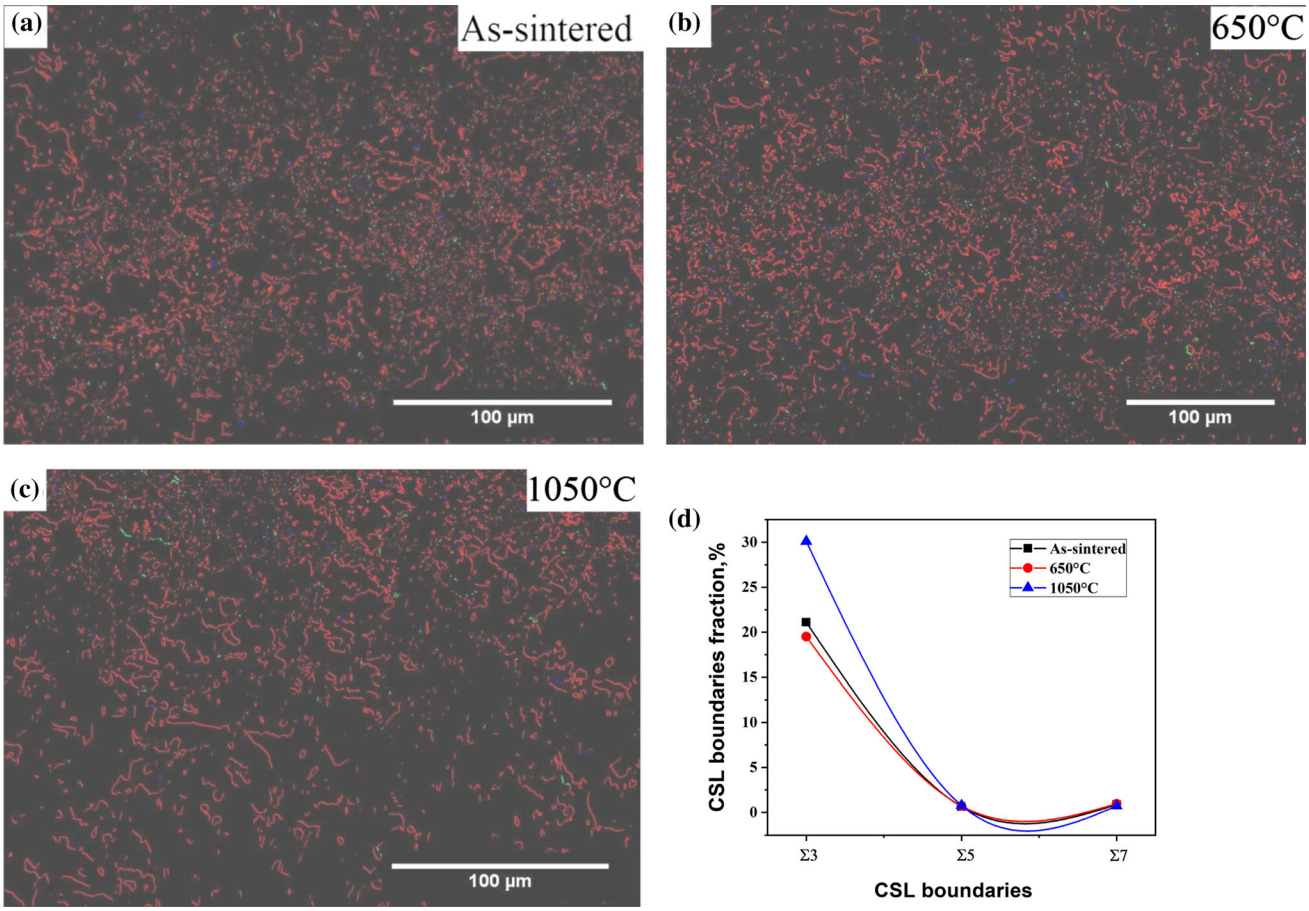

Fig. 4—Coincidence Site Lattice boundary (CSL) map of Alloy 617 ODS (*a*) As-sintered, (*b*) annealed at 650 °C, (*c*) annealed at 1050 °C and (*d*) CSL boundary distribution.

various precipitates, which include both grain boundary and interior of grains. Precipitates are of three types in nature, such as bright and dark blocky and fine globular precipitates. In most cases, bright and dark blocky precipitates are together. Few fine globular precipitates are nucleated at the blocky precipitates, as indicated by arrows. Precipitates in the grain boundary help in inhibiting grain boundary sliding at a higher temperature during creep, and fine precipitates block the dislocation movement. Figures 6(c) and (d) show the BSE micrograph of 650 °C and 1050 °C annealed samples, respectively, it can be seen that similar precipitates are distributed entirely on the matrix. The chemistry of the precipitate is analyzed using EDS, and it is discussed in the following section.

Figure 7 presents the EDS mapping of 1050 °C for the chemistry of different precipitates. Figure 7(a) shows the secondary electron (SE) micrograph of the mapped region. Figures 7(b) through (g) shows the elemental mapping such as Ni, Cr, Mo, C, Al, and O, respectively. Mapping reveals that the bright, blocky precipitates are Mo- and C-rich, dark globular blocky precipitates are Cr- and C-rich, fine precipitates are Al- and O-rich. It has been reported that Alloy 617 ODS consists of precipitates such as Cr-rich $M_{23}C_6$, Mo-rich M_6C, Al- and O-rich Al_2O_3.[18] XRD analysis was carried out for the identification of precipitates which is discussed in the subsequent section. Mapping also shows that the precipitates are discontinuous, and these are advantageous since continuous precipitates will result in cracking and affects fracture toughness. EDS spectrum of the map is represented in Figure 7(h), showing the composition of Alloy 617 ODS resembling Alloy 617 composition.

Figure 8 shows the shape and size analyses of the precipitates. Cr-rich precipitates are of size 0.2 to 2 μm. Mo- and C-rich precipitates are 0.2 to 0.9 μm, and fine Al- and O-rich precipitates are 0.2 to 0.5 μm, respectively. EDS line analysis sample annealed at 1050 °C is shown in Figure 9. Careful attention is paid to cover both the coarse and fine grains. It also supports the EDS mapping result that bright precipitates are rich in Mo and C, dark precipitates are rich in Cr and C, and fine darkest precipitates are rich in Al and O. It has been reported that the submicron-sized Al_2O_3 could provide composite strengthening owing to its low density and high elastic modulus.[15]

Figure 10 shows the XRD pattern of As-sintered and annealed sampled. It is indexed with 617, $M_{23}C_6$, M_6C, and Al_2O_3 peaks, and it substantiates the results of precipitate analysis from SEM micrographs. $M_{23}C_6$ and M_6C were formed, but γ' is not observed in diffraction

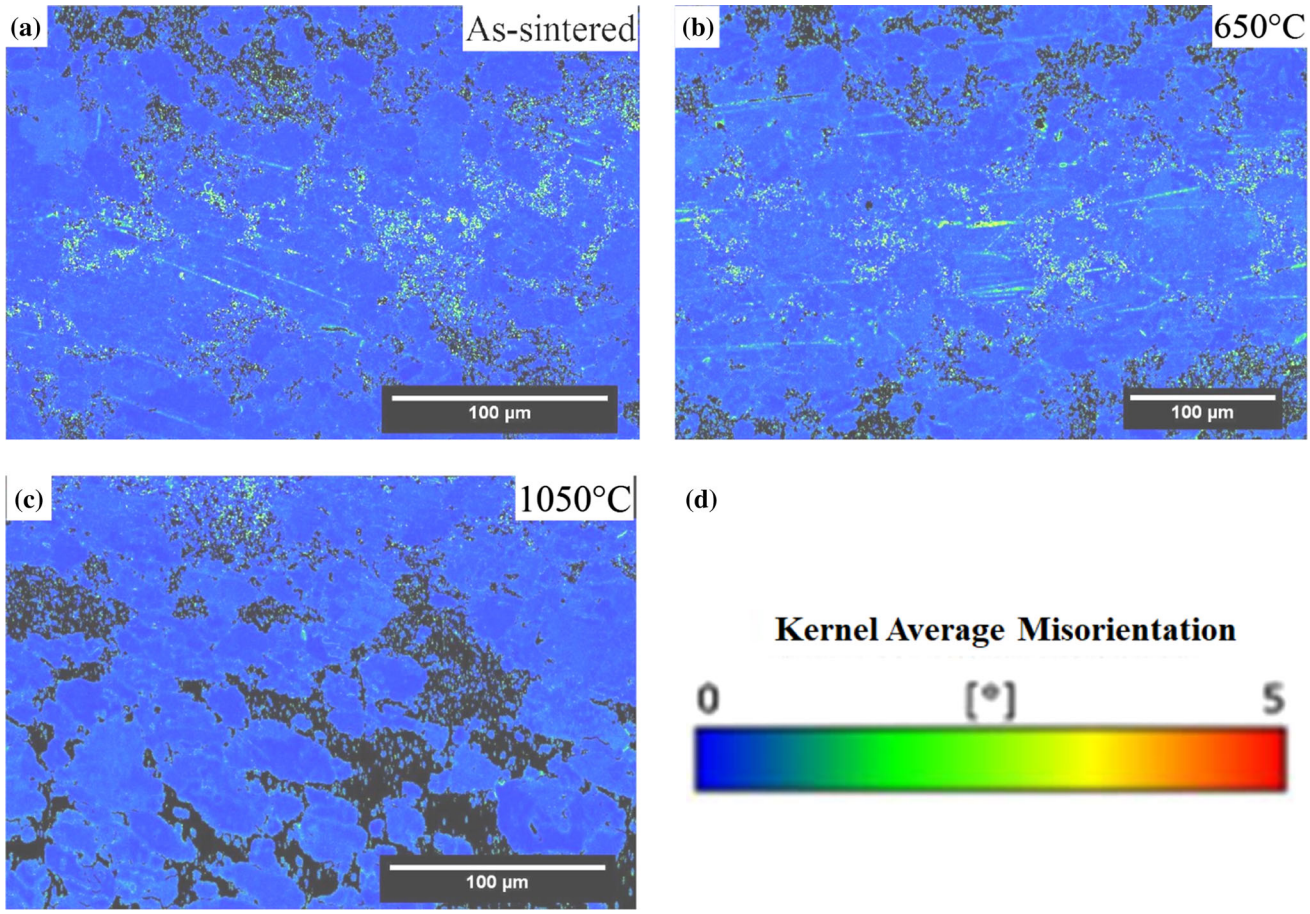

Fig. 5—Kernel average misorientation map (KAM) of Alloy 617 ODS (*a*) As-sintered, (*b*) annealed at 650 °C and (*c*) annealed at 1050 °C with legend in (*d*) (Color figure online).

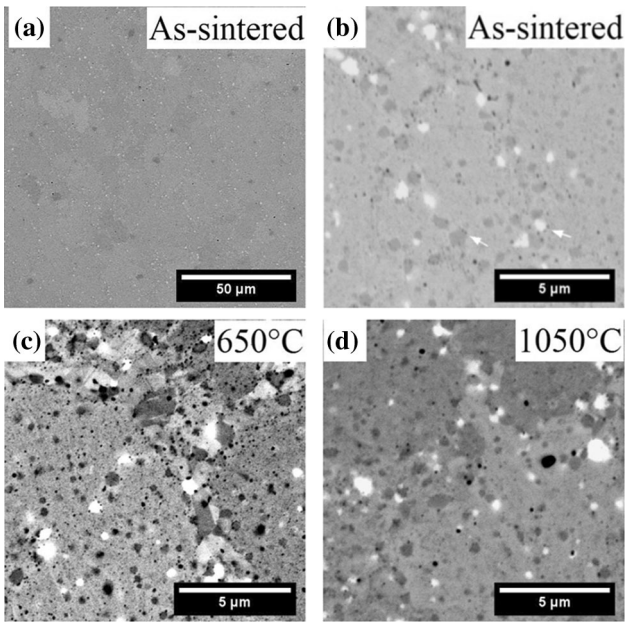

Fig. 6—Back scattered electron (BSE) micrograph of alloy 617 ODS (*a*) As-sintered, (*b*) As-sintered at higher magnification, (*c*) annealed at 650 °C and (*d*) annealed at 1050 °C.

patterns in both As-sintered and annealed samples. If it is formed in a low volume fraction, then it could not be picked by XRD. The other possibility is that the formation of Al_2O_3 could have suppressed the formation of γ' in the alloy. Detailed TEM analysis is carried out in the subsequent section for the confirmation of γ' and also for the dispersoids analysis.

Figure 11(a) shows a Bright Field (BF) micrograph with the presence of fine uniform dispersoids (highlighted with circles) and coarse carbides (highlighted with arrow marks) with a diffraction pattern in the inset. Dispersoid highlighted with the white circle is bcc-$Y_3Al_5O_{12}$ (YAG), and the corresponding indexed selected area diffraction pattern is given in the inset of Figure 11(a). Dispersoid size distribution is shown in Figure 11(b). The average size of dispersoids was found to be 21 nm, and the average dispersoid spacing was estimated using Eq. [1],[15] and it is found to be 51 nm.

$$L = \left[\left(\frac{3\pi}{4f}\right)^{1/2} - 1.64\right] r, \qquad [1]$$

where r is the average radius of dispersoid which is half of the average size of dispersoid, and f is the volume fraction of dispersoids estimated to be 0.055 from the TEM micrograph. Figure 11(c) shows the scanning

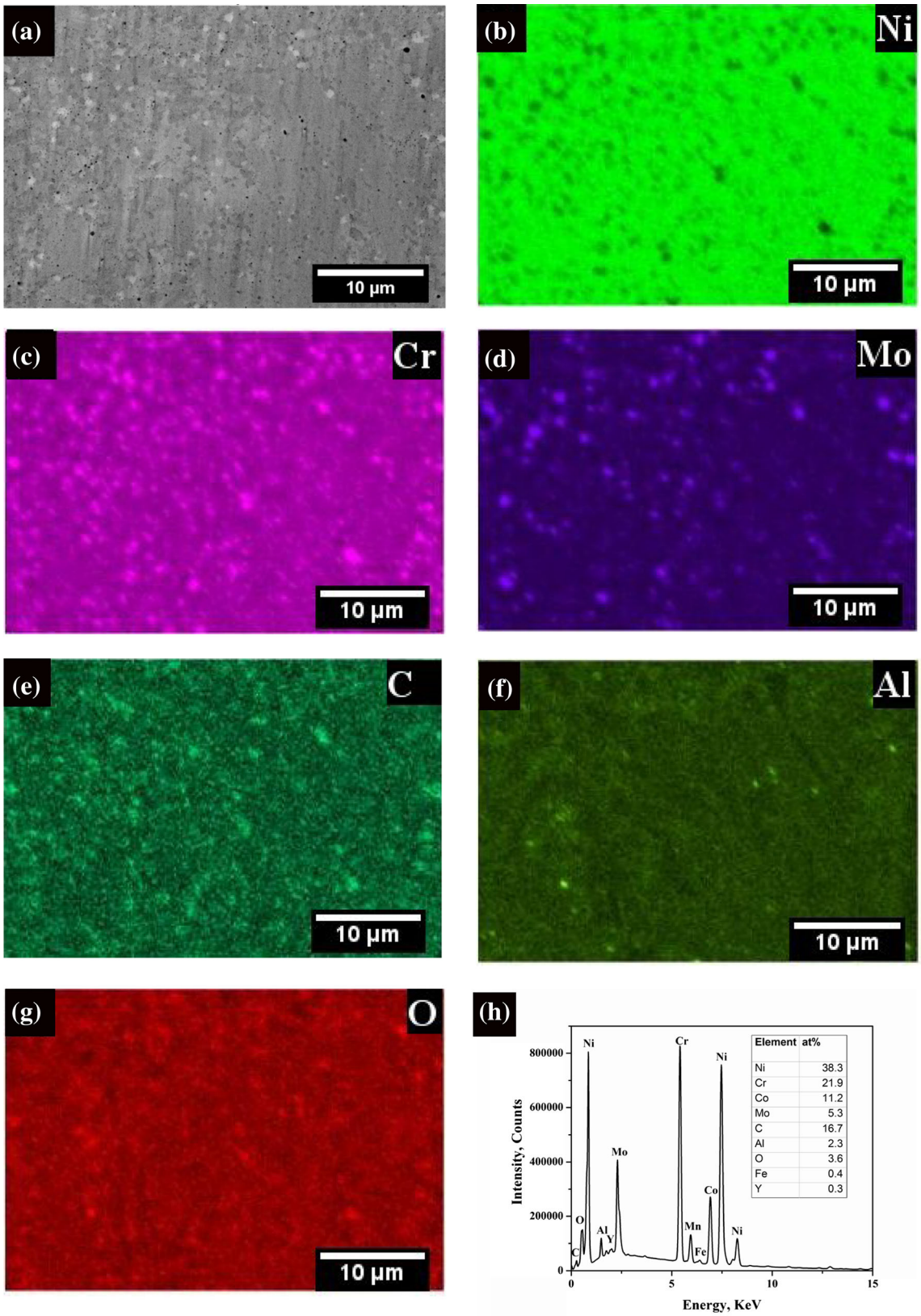

Fig. 7—EDS mapping of alloy 617 ODS annealed at 1050 °C (*a*) secondary electron (SE), micrograph, (*b*) Ni, (*c*) Cr, (*d*) Mo, (*e*) C, (*f*) Al, (*g*) O and (*h*) corresponding spectrum.

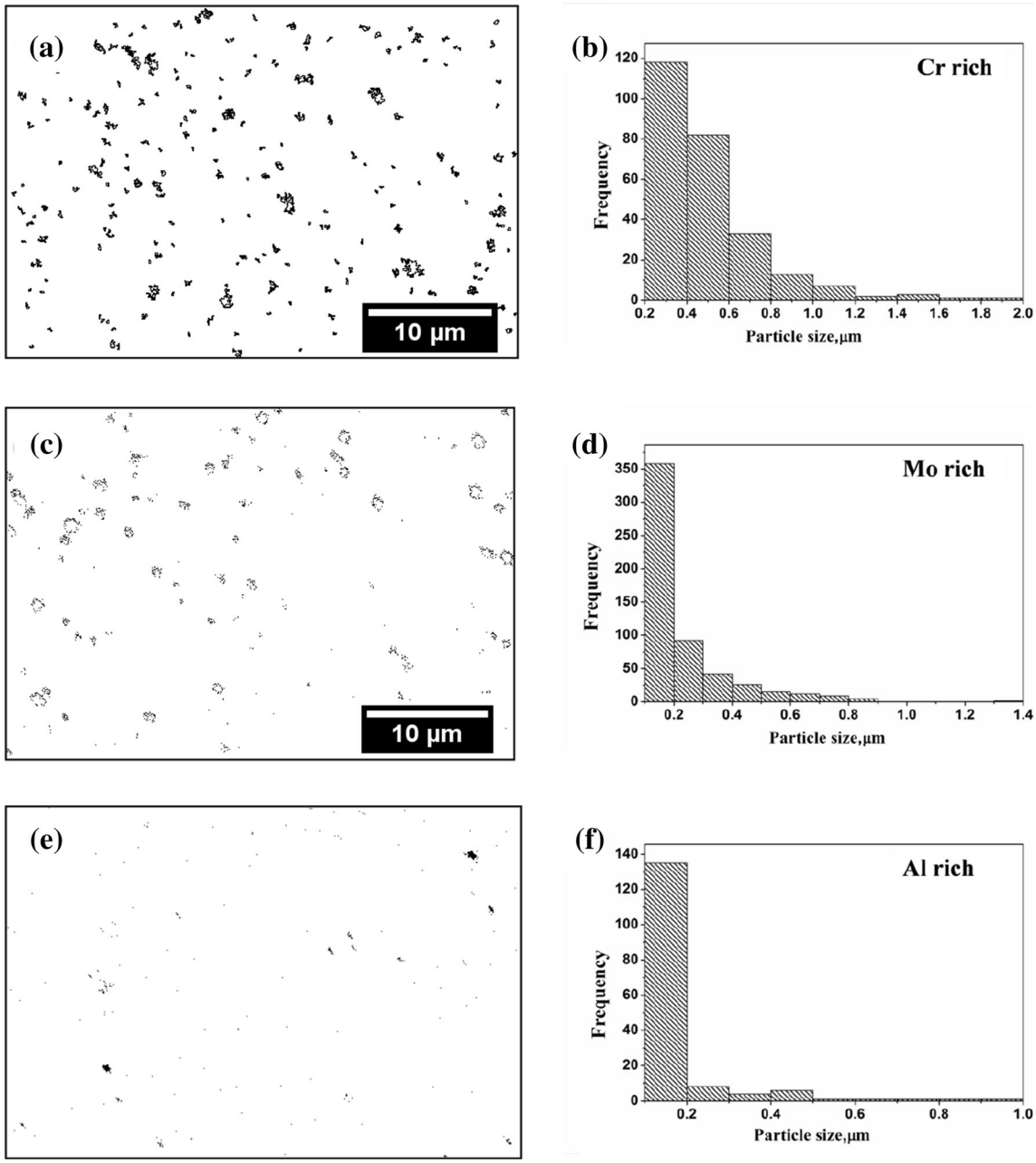

Fig. 8—Precipitate analysis of alloy 617 ODS annealed at 1050 °C (*a*) Cr-rich, (*c*) Mo-rich and (*e*) Al rich and its corresponding size distribution at (*b*), (*d*) and (*f*), respectively.

transmission electron microscopy (STEM) high angle annular dark field (HAADF) image of dispersoids with the corresponding EDS mapping in Figure 11(d). It is observed from the HAADF and EDS mapping that dark faceted particle are Al and O-rich Al_2O_3, dark spherical particles are Y–Al–O complex oxides. Bright contrast particles are rich in Ni, Y, Al and O, observation of such dispersoids is new. Detailed analysis of new dispersoid is currently in progress. A high-resolution aberration-corrected STEM-HAADF image of monoclinic $Y_4Al_2O_9$ (YAM) is shown in Figure 11(e), which is of finer size ~ 10 nm. YAG, YAM and other Y–Al–O complex oxides such as perovskite-$YAlO_3$ (YAP) and hexagonal-$YAlO_3$ (YAH) are reported in nickel-based ODS.[19,32] Figure 11(e) shows the size distribution of dispersoids. Figure 11(f) shows the BF image of a 650 °C annealed sample exhibiting a similar microstructure to that of 1050 °C with carbides and YAG dispersoids. The contribution of dispersoids to the strengthening has been calculated and compared with that of experimental yield strength (YS) in the strengthening mechanism section.

Mechanical property such as stress–strain behaviour is investigated by indentation experiment using spherical indenter of radius 7.6 μm. Ulner *et al.* showed a good agreement of the parameters such as Young's modulus

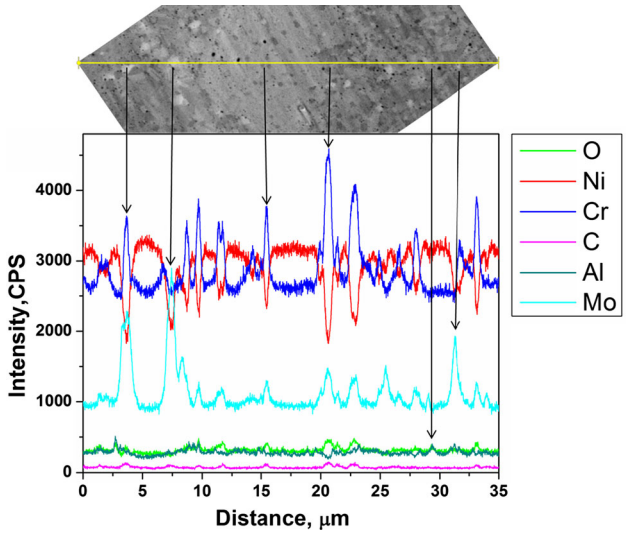

Fig. 9—EDS line scan of Alloy 617 ODS annealed at 1050 °C (Color figure online).

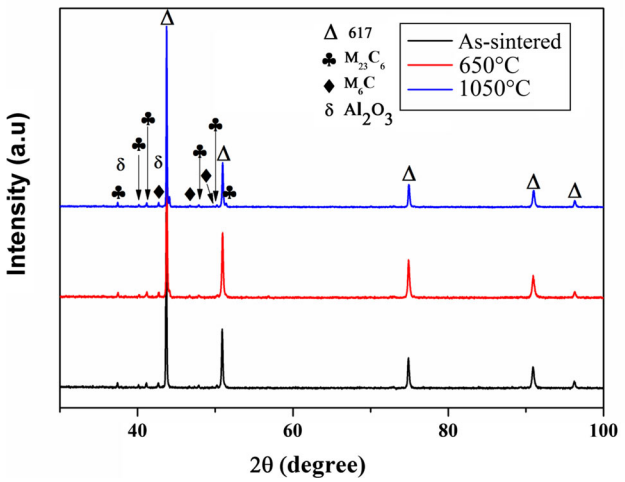

Fig. 10—XRD spectrum of as-sintered Alloy 617 ODS and annealed at different temperature.

and YS as obtained from conventional tensile tests and instrumented indentation tests.[33] Figure 12(a) shows the image quality (IQ) map of Alloy 617 ODS annealed at 1050 °C with an indentation on both coarse and ultra-fine grains (highlighted in white circle). The average load-displacement curve of ultra-fine and coarse grains is shown in Figure 12(b), which clearly reveals that the ultra-fine grains possess higher hardness as compared to the coarse grains. The stress–strain curve generated from instrumented hardness using a neural network module for Alloy 617 ODS and Alloy 617 annealed at 1050 °C is shown in Figure 12(c). Also, the stress–strain curve of Alloy 617 ODS annealed at 650 °C is included in Figure 12(c). Fine and coarse grains of 1050 °C annealed Alloy 617 ODS exhibited YS values of 1298 and 1004 MPa, respectively. When annealed at 650 °C, the fine and coarse grains exhibited relatively higher yield strengths of 1353 and 1122 MPa, respectively. On the other hand, conventional Alloy 617 annealed at 1050 °C for 10 hours showed a YS value of 610 MPa. Due to grain boundary effects,[34,35] the finer grains in the alloy 617 ODS are stronger than the coarse grains. But even then, the relatively softer coarse grains are nearly 50 pct stronger than the Alloy 617. These results highlight the virtue of the dispersion strengthening since the γ' precipitates in the Alloy 617 would have anyway dissolved at 1050 °C, as discussed earlier. Work hardening parameters from the stress–strain plots are explored using swift equation (Eq. [2]),[36] corresponding fit is shown in Figure 12(d) and values are tabulated in Table I.

$$\sigma = K_s(\epsilon_0 + \epsilon_p)^{n_s}, \qquad [2]$$

where ϵ_0 is the amount of pre-strain in the material, and K_S and n_S are the strain-hardening coefficient and exponent, respectively.

The higher K_S value for fine grains, when compared with coarse grains in both of the annealed samples, is attributed to inhibition of dislocation motion due to dispersoid and grain boundary. The observed coarse and fine grains cross-over in stress–strain plot of both the annealed samples show the work hardening nature of coarse grains and this reflects as higher n_S value. From these results, it is also clear that the Alloy 617 ODS retains its strength up to 1050 °C.

IV. DISCUSSION

A. *Microtextural and Microstructural Analysis*

The alloy 617 ODS showed bimodal microstructure in As-sintered and annealed alloys. This distribution may be attributed to the inhomogeneous distribution of plastic deformation in the powder particles, which is inherent nature of ball milling.[22,37] The difference in plastic deformation leads to the difference in stored energy of the powder particles resulting in varying driving forces for recrystallization and grain growth during consolidation at higher temperatures. It needs to be mentioned here that though the basic recrystallization mechanism is well explored, recrystallization in ODS alloys is not yet fully understood. For example, role of grain boundary migration of the recrystallized grains in the presence of oxide particles is debatable. However, the observed bimodal grain structure is considered advantageous due to combination of strength and ductility.[38,39]

IPF analysis also showed weakening of dynamic recrystallization texture in the As-sintered sample. Powder particles are severely cross-rolled during ball milling process which results in shear deformation in different directions. This may affect the recrystallisation behaviour by changing the strain path during SPS. It has been reported that recrystallisation texture in FCC samples is weakened in comparison with straight rolled samples.[40] Thus, the weak texture in As-sintered sample reveals that the processing route has minimum effect on the anisotropic properties.

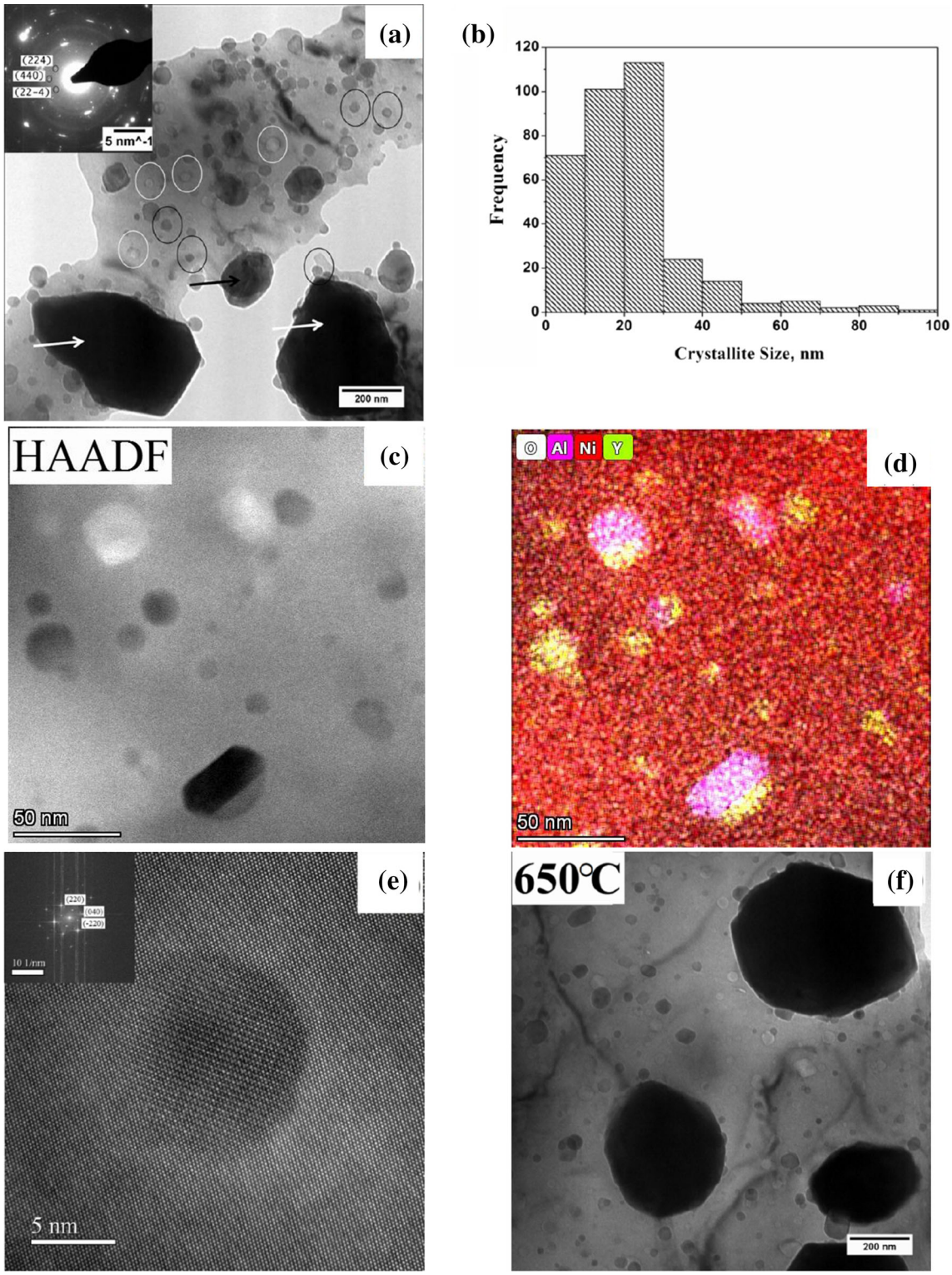

Fig. 11—(*a*) TEM Bright Field (BF) of 1050 °C annealed Alloy 617 ODS with different types of Y–Al–O complex oxide (highlighted with circle) and $Cr_{23}C_6$ precipitates (highlighted with arrow mark), (*b*) corresponding dispersoid size distribution, (*c*) STEM-HAADF of 1050 °C annealed Alloy 617 ODS with corresponding EDS in (*d*), (*e*) high-resolution aberration-corrected STEM-HAADF of $Y_4Al_2O_9$ complex oxide (*f*) BF of 650 °C annealed Alloy 617 ODS.

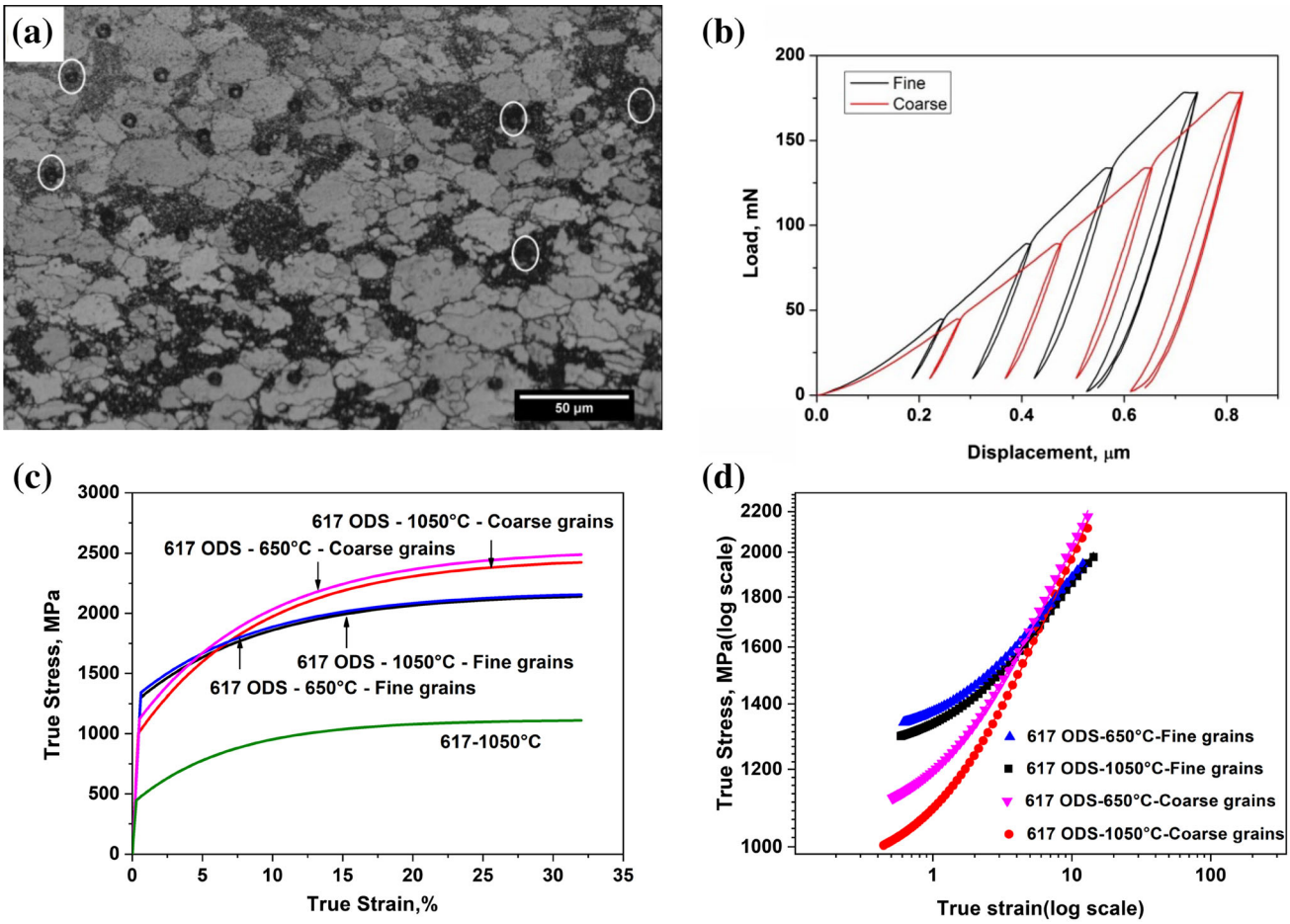

Fig. 12—(*a*) Image quality map of 1050 °C annealed Alloy 617 ODS showing indentation on ultra-fine (highlighted in white circle) and coarse grains, (*b*) average load-displacement curve of respective fine and coarse grains, (*c*) comparison of true stress–strain plots for fine and coarse grains of Alloy 617 ODS annealed at 650 °C, 1050 °C and Alloy 617 annealed at 1050 °C, (*d*) corresponding flow relationship fitted using swift equation.

Table I. Identified Work Hardening Parameters Using Swift Equation

Condition	K_S (MPa)	n_S	ϵ_0
617 ODS—1050 °C—Fine Grain	990	0.24	2.35
617 ODS—1050 °C—Coarse Grain	772	0.38	1.52
617 ODS—650 °C—Fine Grain	992	0.25	2.64
617 ODS—650 °C—Coarse Grain	825	0.36	1.79

On the microstructure aspect, presence of different Y–Al–O complex oxides such as YAM and YAG could be attributed to phase transformation among Y–Al–O complex oxide. Elizabeth *et al.*[41] reported phase transformation from YAM to YAP and to YAG in the temperature range of 1250 °C to 1350 °C by solid-state reaction in the following sequence as represented in equation (3)

$$Y_2O_3 + Al_2O_3 \rightarrow YAM + Al_2O_3 \rightarrow YAP + Al_2O_3 \rightarrow YAG. \quad [3]$$

Zongquing *et al.*[42] reported the possible mechanism of diffusion of Al cation into Y_2O_3 cubic lattice by following reaction in 9Cr-ODS steel as mentioned in Eq. [4]

$$3Y_2O_3 + 10[Al] + 15[O] \rightarrow 2Y_3Al_5O_{12}. \quad [4]$$

Schaffer *et al.* reported the co-existing YAM, YAG, YAP and YAH complex in hot extruded nickel-based ODS alloy MA6000.[32] However, the existing different Y–Al–O complex oxides are fine which is expected to enhance the creep property. The contribution of dispersoids to the YS and the different strengthening mechanisms is discussed in the following section.

B. *Strengthening Mechanism*

The YS of ODS can be expressed as the combination of solid solution strengthening, grain boundary strengthening and dispersion strengthening from nanoscale oxides.[43,44] YS of fine and coarse grains at 1050 °C is estimated and compared with that of the experimental

value obtained from instrumented hardness. YS from solid solution strengthening due to multiple elements in Alloy 617 ODS can be expressed as

$$\sigma_{SS} = K_i C_i^n, \quad [5]$$

where K_i is the solid solution strengthening coefficient for the solute, i and C_i is the atomic fraction of the solute I, n is taken as 0.5.[45] Cr, Co and Mo are the substitution solid solution strengtheners, and the corresponding solid solution strengthening coefficient values are $K_{cr} = 337\ \text{MPa}/\sqrt{\text{at pct}}$, $K_{Co} = 39.4\ \text{MPa}/\sqrt{\text{at pct}}$ and $K_{Mo} = 1015\ \text{MPa}/\sqrt{\text{at pct}}$, respectively.[46] The composition of Cr, Co and Mo are 21.9, 11.2 and 5.3 at pct, respectively, taken from the EDS which is shown in inset of Figure 7(e). Using equation (5), the value of σ_{SS} is found to be 405 MPa.

Yield strength from Hall–Petch relationship,

$$\sigma_{HP} = \sigma_0 + K_{HP} D^{-1/2}, \quad [6]$$

where σ_0 is the friction stress, K_{HP} is the Hall–Petch constant, and D represents the grain size. σ_0 and K_{HP} of Ni taken from literature for a grain size of 470 nm is 8 MPa and 5538 $\text{MPanm}^{1/2}$,[47] respectively. In the current study measured ultra-fine grain size was 500 nm. With the above parameters, σ_{HP} is estimated as 255 MPa from Eq. [6].

The higher yield strength in ODS is attributed to the presence of fine and uniformly distributed nanoscale oxides. Dispersoid strengthening is calculated using Eq. [7],[48] given below by taking the dispersoid size and average distance between them into account,

$$\sigma_D = 0.9\,M \frac{[\ln(\pi d/b)]^{3/2}}{[\ln(L/b)]^{1/2}} \frac{[Gb/4\pi(1-v)]}{[L-(\pi d/4)]}, \quad [7]$$

where $v = 0.3$ is the Poisson's ratio, G is the shear modulus, $b = 0.25$ nm is the modulus of burger vector,[47] L and d represents the mean spacing between dispersoid and dispersoid size, respectively. The average dispersoids size and the average distance between the dispersoids determined from the TEM analysis were 21 and 51 nm, respectively.

Shear modulus is calculated from the relation,

$$G = \frac{E}{2(1+v)}, \quad [8]$$

where E is elastic modulus. From the instrumented hardness, E was found to be 220 GPa. G is calculated as 83 GPa using Eq. [8]. Feeding the values of L, b, d, v, and G in Eq. [3], σ_D was found to be 531 MPa.

YS estimated from solid solution strengthening, Hall–Petch strengthening and dispersoid strengthening is found to be 1191 MPa which is comparable to that of experimental YS value of 1298 MPa of alloy 617 ODS annealed at 1050 °C. Thus Alloy 617 ODS derives strength from Hall–Petch strengthening and dispersion strengthening in addition to solid solution strengthening. Whereas the conventional Alloy 617 derives its strength majorly from solid solution strengthening.

V. CONCLUSION

Alloy 617 ODS was synthesized by high energy ball milling, consolidated by SPS technique and followed by annealing at 650 °C and 1050 °C. Microstructural and micro-texture characterization of both As-sintered and annealed samples were carried out. Following are the important results from the characterization.

1. Both As-sintered and annealed specimen exhibited bimodal grain structure which is advantageous with fine grains providing strength by Hall–Petch relationship, and coarse grains provide ductility.
2. In As-sintered specimen, weak ⟨100⟩ texture parallel to compression axis due to dynamic recrystallization during the SPS process. 650 °C annealed sample exhibited weak ⟨111⟩ annealing texture parallel to compression axis. Texture randomized at 1050 °C annealed samples.
3. $M_{23}C_6$, M_6C, Al_2O_3 precipitates are present in the matrix of both As-sintered and annealed samples in addition to the presence of fine uniform $Y_3Al_5O_{12}$, $Y_4Al_2O_9$, and new complex oxide rich in Ni, Y, Al and O. Alloy 617 ODS derives its strength from both precipitates and dispersoids in addition to solid solution strengthening element. γ' is not observed due to Al_2O_3 and Y–Al-O complex oxide formation.
4. Alloy 617 ODS annealed at 1050 °C displayed higher yield strength in comparison with conventional Alloy 617 under similar condition due to the presence of Y–Al–O dispersoids. Coarse grains work hardened in both the annealed samples and it is manifested as cross-over in stress–strain plot.

ACKNOWLEDGMENTS

The authors thank Dr. A. K. Bhaduri, Director, Indira Gandhi Center for Atomic Research (IGCAR), Dr. Shaju K. Albert, Director, Metallurgy and Materials Group Dr. S. Raju, Associate Director, Materials Characterization Group for their constant support and encouragement during the course of this work. Authors gratefully acknowledge the experimental support provided by UGC-DAE-CSR Kalpakkam node, IGCAR and Madras Regional Purchase Unit for experimental facility and one of the authors (Sivakumar) acknowledges DAE, India for the fellowship.

REFERENCES

1. J.J. Stephens and W.D. Nix: *Metall. Trans. A*, 1985, vol. 16, pp. 1307–324.
2. L.J. Park, H.J. Ryu, S.-H. Hong, and Y.G. Kim: *Adv. Perform. Mater.*, 1998, vol. 5, pp. 279–90.
3. N. Oono, S. Ukai, S. Kondo, O. Hashitomi, and A. Kimura: *J. Nucl. Mater.*, 2015, vol. 465, pp. 835–39.
4. J. Jang, T.K. Kim, C.H. Han, H.-K. Min, S.-H. Jeong, and D.H. Kim: *Procedia Eng.*, 2013, vol. 55, pp. 284–88.
5. F Masoumi, M Jahazi, D Shahriari, and J Cormier: *J. Alloys Compd.*, 2016, vol. 658, pp. 981–95.

6. V Swamy, NA Dubrovinskaya, and LS Dubrovinsky: *J. Mater. Res.*, 1999, vol. 14, pp. 456–59.
7. M. Sivakumar, A. Dasgupta, C. Ghosh, D. Sornadurai, and S. Saroja: *Adv. Powder Technol.*, 2019, vol. 30, pp. 2320–29.
8. M. Sivakumar and A. Dasgupta: *Mater. Charact.*, 2019, vol. 157, p. 109883.
9. C-L Chen and Y-M Dong: *Mater. Sci. Eng. A*, 2011, vol. 528, pp. 8374–80.
10. M.A. Auger, V. De Castro, T. Leguey, A. Muñoz, and R. Pareja: *J. Nucl. Mater.*, 2013, vol. 436, pp. 68–75.
11. I. Hilger, X. Boulnat, J. Hoffmann, C. Testani, F. Bergner, Y. De Carlan, F. Ferraro, and A. Ulbricht: *J. Nucl. Mater.*, 2016, vol. 472, pp. 206–214.
12. C. Balázsi, F. Gillemot, M. Horváth, F. Wéber, K. Balázsi, F.C. Sahin, Y. Onüralp, and Á. Horváth: *J. Mater. Sci.*, 2011, vol. 46, pp. 4598–4605.
13. X. Boulnat, D. Fabregue, M. Perez, M.-H. Mathon, and Y. De Carlan: *Metall. Mater. Trans. A*, 2013, vol. 44A, pp. 2461–2465.
14. C. Heintze, M. Hernández-Mayoral, A. Ulbricht, F. Bergner, A. Shariq, T. Weissgärber, and H. Frielinghaus: *J. Nucl. Mater.*, 2012, vol. 428, pp. 139–146.
15. S. Pasebani, A.K. Dutt, J. Burns, I. Charit, and R..S Mishra: *Mater. Sci. Eng. A*, 2015, vol. 630, pp. 155–69.
16. Q. Tang, S. Ukai, N. Oono, S. Hayashi, B. Leng, Y. Sugino, W. Han, and T. Okuda: *Mater. Trans.*, 2012, vol. 53, pp. 645–51.
17. Y.B. Chun, X. Mao, C.H. Han, and J. Jang: *Mater. Sci. Eng. A*, 2017, vol. 706, pp. 161–71.
18. X. Mao, Y.-B. Chun, C.-H. Han, and J. Jang: *J. Mater. Sci.*, 2017, vol. 52, pp. 13626–35.
19. M. Wang, H.N. Han, C.H. Han, W.-G. Kim, and J. Jang: *Mater. Charact.*, 2018, vol. 139, pp. 11–18.
20. J.S. Benjamin: *Metall. Trans.*, 1970, vol. 1, pp. 2943–51.
21. C. Suryanarayana: *Prog. Mater. Sci.*, 2001, vol. 46, pp. 1–184.
22. X. Boulnat, M. Perez, D. Fabregue, T. Douillard, M.-H. Mathon, and Y. De Carlan: *Metall. Mater. Trans. A*, 2014, vol. 45A, pp. 1485–97.
23. Z. Dapeng, L. Yong, L. Feng, W. Yuren, Z. Liujie, and D. Yuhai: *Mater. Lett.*, 2011, vol. 65, pp. 1672–74.
24. S.L. Shang, C.L. Zacherl, H.Z Fang, Y. Wang, Y. Du, and Z.K. Liu: *J. Phys. Condens. Matter*, 2012, vol. 24, p. 505403.
25. E.A. Holm and S.M. Foiles: *Science (80–)*, 2010, vol. 328, pp. 1138–41.
26. P.S. Singh, D. Chen, L. Shao, Y.N. Picard, and M.P. de Boer: *J. Appl. Phys.*, 2019, vol. 126, p. 175901.
27. S.P. Coryell, K.O. Findley, M.C. Mataya, and E. Brown: *Metall. Mater. Trans. A*, 2012, vol. 43A, pp. 633–649.
28. N. Dudova, A. Belyakov, T. Sakai, and R. Kaibyshev: *Acta Mater.*, 2010, vol. 58, pp. 3624–32.
29. M. Wang, C. Sun, M.W. Fu, Z. Liu, and C. Wang: *Mater. Des.*, 2020, vol. 188, p. 108429.
30. P.P. Bhattacharjee, M. Joshi, V.P. Chaudhary, J.R. Gatti, and M. Zaid: *Metall. Mater. Trans. A*, 2013, vol. 44A, pp. 2707–716.
31. V.N. Danilenko, D.V. Bachurin, and A.A Nazarov: *Rev. Adv. Mater. Sci.*, 2018, vol. 55, pp. 69–77.
32. G.B. Schaffer, M.H. Loretto, R.E. Smallman, and J.W. Brooks: *Acta Metall.*, 1989, vol. 37, pp. 2551–58.
33. D. Klötzer, C. Ullner, E. Tyulyukovskiy, and N. Huber: *J. Mater. Res.*, 2006, vol. 21, pp. 677–84.
34. J.H. Schneibel, M. Heilmaier, W. Blum, G. Hasemann, and T. Shanmugasundaram: *Acta Mater.*, 2011, vol. 59, pp. 1300–08.
35. N. Hansen: *Scr. Mater.*, 2004, vol. 51, pp. 801–06.
36. H. Swift: *J. Mech. Phys. Solids*, 1952, vol. 1, pp. 1–18.
37. B. Mouawad, X. Boulnat, D. Fabrègue, M. Perez, and Y. De Carlan: *J. Nucl. Mater.*, 2015, vol. 465, pp. 54–62.
38. V.A. Pozdnyakov: *Tech. Phys. Lett.*, 2007, vol. 33, pp. 1004–06.
39. Y. Wang, M. Chen, F. Zhou, and E. Ma: *Nature*, 2002, vol. 419, pp. 912–15.
40. L. Wang, X. Chen, T. Luo, H. Ni, L. Mei, P. Ren, Q. Liu, Y. Ding, and L. Zhao: *Rev. Adv. Mater. Sci.*, 2020, vol. 59, pp. 252–63.
41. E.R. Kupp, S. Kochawattana, S.-H. Lee, S. Misture, and G.L. Messing: *J. Mater. Res.*, 2014, vol. 29, pp. 2303–311.
42. X. Zhou, Z. Ma, L. Yu, Y. Huang, H. Li, and Y Liu: *J. Mater. Sci.*, 2019, vol. 54, pp. 7893–907.
43. A. De Vaucorbeil, W.J. Poole, and C.W. Sinclair: *Mater. Sci. Eng. A*, 2013, vol. 582, pp. 147–54.
44. H. Xu, Z. Lu, D. Wang, and C. Liu: *Nucl. Eng. Technol.*, 2017, vol. 49, pp. 178–88.
45. M.R. Ahmadi, E. Povoden-Karadeniz, L. Whitmore, M. Stockinger, A. Falahati, and E. Kozeschnik: *Mater. Sci. Eng. A*, 2014, vol. 608, pp. 114–22.
46. H.A. Roth, C.L. Davis, and R.C. Thomson: *Metall. Mater. Trans. A*, 1997, vol. 28A, pp. 1329–35.
47. W. He, F. Liu, L. Tan, L. Huang, Y. Nie, G. Wang, X. Zhan, and Z. Qin: *Mater. Today Commun.*, 2021, vol. 26, p. 101921.
48. M. De Sanctis, A. Fava, G. Lovicu, R. Montanari, M Richetta, C Testani, and A Varone: *Metals (Basel)*, 2017, vol. 7, p. 283.